Majorana corner modes and tunable patterns in an altermagnet heterostructure

Yu-Xuan Li and Cheng-Cheng Liu [*]

*Centre for Quantum Physics, Key Laboratory of Advanced Optoelectronic Quantum Architecture and Measurement (MOE),
School of Physics, Beijing Institute of Technology, Beijing 100081, China*

The mutual competition and synergy of magnetism and superconductivity provide us with a very valuable opportunity to access topological superconductivity and Majorana fermions. Here, we devise a heterostructure consisting of an s-wave superconductor, a two-dimensional topological insulator, and an altermagnet, which is classified as the third magnet and featured by zero magnetization but spin polarization in both real and reciprocal spaces. We find that the altermagnet can induce mass terms at the edges that compete with electron pairing, and mass domains are formed at the corners of the sample, resulting in zero-energy Majorana corner modes (MCMs). The presence or absence of MCMs can be engineered by only changing the direction of the Néel vector. Moreover, uniaxial strain can effectively manipulate the patterns of the MCMs, such as moving and interchanging MCMs. Experimental realization, remarkable advantages of our proposal, and possible braiding are discussed.

Introduction. In the past decade, Majorana zero modes (MZMs) have been extensively researched as building blocks for topological quantum computation [1–6]. Topological superconductors have gained tremendous attention in both experimental and theoretical settings [1,7–11] as a promising platform for the realization of MZMs. The key feature that differentiates topological superconductors from trivial ones is the presence of MZMs at the boundaries of the system [12–14] or the core of the vortices [15–18].

The higher-order topological states of matter have extended our understanding of topological states [19–28] and provided a new path for the realization of MZMs [29–50]. Compared with first-order conventional topological superconductors, higher-order topological superconductors (HOTSCs) have a special "bulk-edge" correspondence. Specifically, the codimension (d_c) of edge states or end states in conventional topological superconductors is 1, while the d_c of hinge states or corner states in HOTSCs is equal to or greater than 2. Previous studies have proposed several heterojunction systems to realize HOTSCs with MZMs, such as utilizing topological p-wave superconductors [36], unconventional or conventional superconductor/topological insulator heterojunctions [34,35,47], and ferromagnetic heterojunctions [32,42]. Although progress has been made in the study of HOTSCs, platforms for tunable MZMs are still difficult to achieve.

Recently, a new magnetic phase dubbed altermagnets [51,52] was discovered in several materials, such as RuO_2 [53,54], Mn_5Si_3 [55], and KRu_4O_8 [54], which breaks the time-reversal symmetry (TRS) despite having zero net magnetization. Interestingly, altermagnets with nonrelativistic highly anisotropic spin splitting [54] are used to explore some interesting properties [51,56–63], such as finite-momentum Cooper pairing, Andreev reflection, Hall effect, etc.

A natural question is whether we can use the highly anisotropic spin splitting and zero magnetization unique to altermagnets to design and optimize topological superconductivity, especially higher-order topological superconductivity and the hallmark Majorana modes.

In this work, we investigate the combination of altermagnets with superconductor/topological insulator heterojunctions, as illustrated in Fig. 1(a), and give an affirmative answer to the above question. There are several forms of spin splitting in altermagnets with different symmetries, such as d-wave,
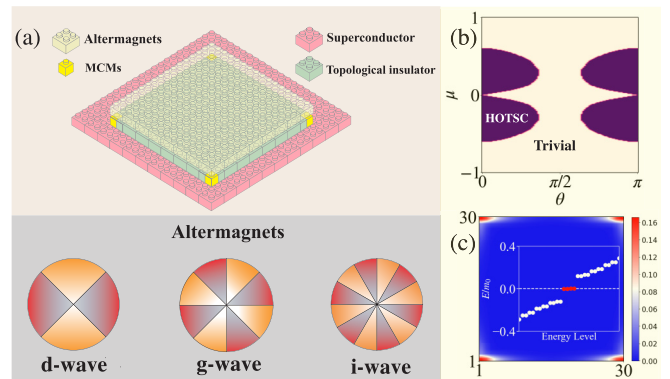

FIG. 1. (a) Schematic of the proposed altermagnet heterostructure. A two-dimensional topological insulator is sandwiched between an s-wave superconductor and an altermagnet. The emerging MZMs are localized at the corners. Altermagnets have various spin-momentum locking with the even-parity waveform, such as d wave, g wave, and i wave. (b) The phase diagram in the plane of Néel vector polar angle θ and chemical potential μ. (c) The real-space wave-function distribution with one MZM localized at each corner. (Inset) Plot of the several eigenvalues near zero energy. The common parameters are $m_0 = 1.0$, $t_x = A_x = A_y = 1.0$, $t_y = 0.5$, $\Delta_0 = 0.5$, and $J_0 = 1.0$.

*ccliu@bit.edu.cn

g-wave, and *i*-wave [54]. Without loss of generality, we consider an altermagnets with *d*-wave magnetism as an example, and the other symmetries have a similar analysis procedure [64]. Our findings demonstrate that altermagnetism can drive the system into a HOTSC phase, resulting in the emergence of MZMs at the corners of the system, i.e., Majorana corner modes (MCMs). By adjusting the chemical potential or varying the direction of the Néel vector, which are both readily achieved experimentally, we can create or annihilate a pair of MCMs. Furthermore, combined with uniaxial stress, we can move and switch MCMs arbitrarily, offering flexible adjustability for further research.

Model. We begin with a general form of the superconducting mean-field Hamiltonian $\mathcal{H} = \frac{1}{2} \sum_{\boldsymbol{k}} \Psi_{\boldsymbol{k}}^{\dagger} H^{\text{BdG}}(\boldsymbol{k}) \Psi_{\boldsymbol{k}}$, where the Nambu spinor basis $\Psi_{\boldsymbol{k}}^{\dagger} = (c_{\boldsymbol{k}\alpha}^{\dagger}, c_{-\boldsymbol{k}\alpha})$, with $c_{\boldsymbol{k}\alpha}^{\dagger} (c_{\boldsymbol{k}\alpha})$ representing the fermion creation (annihilation) operator for the α degree of freedom. The corresponding Bogoliubov–de Gennes (BdG) Hamiltonian is given by

$$H^{\text{BdG}}(\boldsymbol{k}) = \begin{pmatrix} H_0(\boldsymbol{k}) - \mu\Gamma_{00} & -i\Gamma_{20}\Delta_0 \\ i\Gamma_{20}\Delta_0 & \mu\Gamma_{00} - H_0^*(-\boldsymbol{k}) \end{pmatrix},$$

$$H_0(\boldsymbol{k}) = M(\boldsymbol{k})\Gamma_{03} + A_x \sin k_x \Gamma_{21} + A_y \sin k_y \Gamma_{11}$$
$$+ J(\boldsymbol{k})\boldsymbol{s} \cdot \boldsymbol{n} \otimes \sigma_x. \tag{1}$$

$\Gamma_{ij} = s_i \otimes \sigma_j$ with s_j and σ_j acting on the spin $(\uparrow, \downarrow)$ and orbital (a, b) degree of freedom, respectively. The Néel vector, represented by a unit vector $\boldsymbol{n} = (\sin\theta\cos\varphi, \sin\theta\sin\varphi, \cos\theta)$, can be rotated experimentally [65]. The first line of the Hamiltonian $H_0(\boldsymbol{k})$ can describe the conventional topological insulator with a nontrivial $\mathcal{Z}_2$ invariant [66] with $M(\boldsymbol{k}) = (m_0 - t_x \cos k_x - t_y \cos k_y)$, while the second line denotes the *d*-wave altermagnetism with $J(\boldsymbol{k}) = J_0(\cos k_x - \cos k_y)$ [52,54]. Throughout this work we use the lattice constants as units, and take all the parameters $m_0, t_{x(y)}, A_{x(y)}, J_0$, and Δ_0 positive. When we ignore the altermagnetism term in the normal states, the Hamiltonian depicts a two-dimensional topological insulator with time-reversal symmetry [67]. The TRS operation is given by $\mathcal{T} = is_y\mathcal{K}$, where $\mathcal{K}$ is the complex conjugate. When the "mass-ring" $M(\boldsymbol{k}) = 0$ [where the $M(\boldsymbol{k})$ term changes sign] of the topological insulator contains an odd number of time-reversal-invariant momentums (TRIMs), the system has gapless helical edge states protected by the TRS [68].

Zero-energy MCMs. When proximitized with an *s*-wave superconductor and an altermagnet, the helical edge states will be gapped by breaking the $U(1)$ charge conservation symmetry and TRS, respectively. The interplay of the *s*-wave pairing and altermagnet order parameter will drive the system into the HOTSC phase. We consider the general case and choose the chemical potential and Néel vector as variable parameters, finding that both have significant effects on the MCMs, as illustrated in the phase diagram [Fig. 1(b)]. One can find that there are no MCMs when the Néel vector is close to the in-plane direction. On the contrary, when the Néel vector has a certain out-of-plane component, it favors the formation of MCMs. In the HOTSC phase, there is one MCM at each corner, as shown in Fig. 1(c).
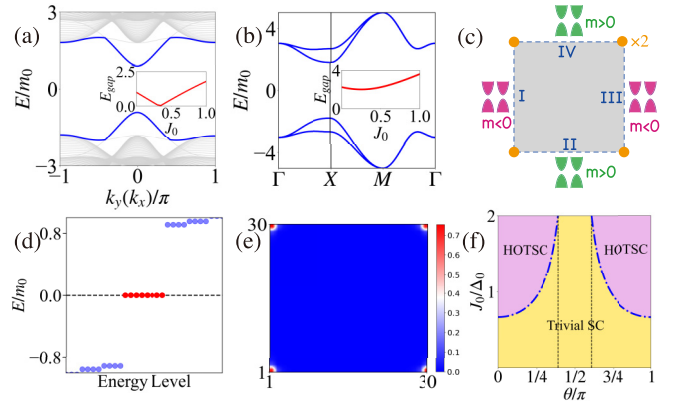

FIG. 2. (a) Quasiparticle spectrum for a cylindrical geometry. In the presence of altermagnetism and electron pairing, the otherwise-helical edge states open a gap. The inset shows the variation of the edge gap with order parameter strength J_0 of altermagnets. The closure of the edge states at the critical $J_0 = J_0^c$ indicates a topological phase transition at the boundary. (b) Bulk bands along the high-symmetry path at $J_0 = 1.0$. The inset shows the evolution of the bulk gap with J_0, and no bulk gap closure is found. (c) Schematic demonstrating the Dirac mass terms of adjacent edges with opposite signs, forming two domain walls. I, II, III, and IV donate four edges. (d) The real-space energy spectrum of an open-boundary square structure of size $L_x = L_y = 30$. Eight MZMs emerge (red dots). (e) The distribution of the MZM wave function in real space. (f) The phase diagram in the plane of the azimuth angle θ and J_0. The blue dotted lines mark the phase boundary. The common parameters are $m_0 = 1.0$, $t_x = t_y = A_x = A_y = 2.0$, and $\Delta_0 = 0.5$.

To get an intuitive picture of the MCMs, we fix the chemical potential $\mu = 0$ and Néel vector along the z direction ($\theta = 0$) for simplicity. When $\Delta_0 \neq 0$, $J_0 = 0$, the TRS of the system still holds, but the broken $U(1)$ symmetry makes the helical edge states open a gap, and the system is a trivial superconductor [47]. With the altermagnetism turned on and the increase of J_0, the edge-state gap along the direction of $x(y)$ will be closed and reopened again, as shown in Fig. 2(a). However, during the process the bulk state is always fully gapped [Fig. 2(b)]. This indicates a possible higher-order topological phase transition [28], which can be made more clearly by the edge theory in the next section. After the phase transition, eight MCMs appear with two MCMs at each corner, which are characteristic of the HOTSC phase, as shown in Figs. 2(d) and 2(e). We will see later that the doubling of MCMs here is due to the additional symmetry brought about by the zero chemical potential. In addition, adjusting the Néel vector will affect the location of higher-order topological phase transitions. With the chemical potential $\mu = 0$, we analytically obtained the phase diagram in the plane of the amplitude J_0 and the polar angle θ of the altermagnetic order parameter, as plotted in Fig. 2(f).

Edge theory. The appearance of MCMs after the higher-order topological phase transition can be intuitively understood by edge theory. For simplicity, we first consider the case of the chemical potential $\mu = 0$ and Néel vector along the z axis [69]. We expand the Hamiltonian $H^{\text{BdG}}(\boldsymbol{k})$ in Eq. (1)

around $\boldsymbol{\Gamma} = (0, 0)$ to the second order,

$$H^{\text{BdG}}(\boldsymbol{k}) = \left(m + \frac{t_x}{2}k_x^2 + \frac{t_y}{2}k_y^2\right)\Lambda_{303} + A_x k_x s_y \Lambda_{321}$$
$$+ A_y k_y \Lambda_{011} - \frac{J_0}{2}(k_x^2 - k_y^2)\Lambda_{331} + \Delta_0 \Lambda_{220}, \quad (2)$$

with $\Lambda_{ijk} = \tau_i \otimes \Gamma_{jk}$, and τ_i are Pauli matrices in the particle-hole space. The parameter $m = m_0 - t_x - t_y < 0$ ensures that the mass ring contains the odd number of TRIMs [68]. To distinguish the boundaries, we label the four boundaries using I, II, III, and IV, respectively, as shown in Fig. 2(c). We first focus on edge I. The momentum k_x is replaced by $-i\partial_x$, and the Hamiltonian can be decomposed into two parts $H = H_0 + H'$, which are denoted as $H_0(-i\partial_x, k_y) = (m - t_x\partial_x^2/2)\Lambda_{303} - iA_x\partial_x\Lambda_{321}$ and $H'(-i\partial_x, k_y) = A_y k_y \Lambda_{011} + J_0\partial_x^2/2\Lambda_{331} + \Delta_0\Lambda_{220}$, respectively. We solve the eigenequation $H_0\psi_\alpha(x) = E_\alpha\psi_\alpha(x)$, satisfying the boundary condition $\psi_\alpha(0) = \psi_\alpha(+\infty) = 0$, and obtain four $E_\alpha = 0$ solutions [64]. The perturbation part H' is projected onto the bases ψ_α and reads as $H_I = A_y k_y \eta_z - M_I \eta_y \gamma_y + J_I \eta_x \gamma_z$, where the Pauli matrices γ_i, η_j are defined in the four zero-energy-states ψ_α space. The mass terms $J_I = J_0 m/t_x$ and $M_I = \Delta_0$ originate from the altermagnetism and electron pairing, respectively [64].

The effective Hamiltonian on the other edges (II-IV) can be obtained similarly [64]. For the convenience of the discussion, we define the edge coordinates l counterclockwise, and the effective Hamiltonian can be compactly written as

$$H^{\text{edge}}(l) = -iA(l)\eta_z\partial_l + M(l)\eta_y\gamma_y + J(l)\eta_x\gamma_z, \quad (3)$$

where for the edge coordinate $l = \{\text{I-IV}\}$, $A(l) = \{A_y, A_x, A_y, A_x\}$, $M(l) = \{-\Delta_0, \Delta_0, \Delta_0, -\Delta_0\}$, and $J(l) = \{J_0 m/t_x, -J_0 m/t_y, J_0 m/t_x, -J_0 m/t_y\}$, respectively. From Eq. (3) one can obtain that the Dirac masses originated from s-wave pairing and the altermagnets are commutable, indicating that they compete with each other on the edges. The boundary energy spectrum of Eq. (3) reads as $E_{\text{I,III}}^{\text{edge}}(k_y) = \pm\sqrt{(A_y k_y)^2 + (\mp\Delta_0 \pm J_{\text{I(III)}})^2}$, $E_{\text{II,IV}}^{\text{edge}}(k_x) = \pm\sqrt{(A_x k_x)^2 + (\pm\Delta_0 \pm J_{\text{II(IV)}})^2}$. One can find that as J_0 increases, the gap of the edge state decreases, and at the critical value $J_0^c m/t_{x(y)} = \pm\Delta_0$, the gap closes that corresponds to the higher-order topological phase transition and is consistent with the numerical results of Fig. 2.

Furthermore, we can decompose the Hamiltonian (3) as $H = H^+ \oplus H^-$ with the help of a conserved quantity $\Pi = \eta_z\gamma_x$. The effective Hamiltonian for two subspaces with $\Pi = \pm 1$ can be obtained as

$$H^+ = iA(l)\tilde{\eta}_z\partial_l + \tilde{M}^+(l)\tilde{\eta}_x,$$
$$H^- = iA(l)\tilde{\eta}_z\partial_l + \tilde{M}^-(l)\tilde{\eta}_x, \quad (4)$$

with Pauli matrices $\tilde{\eta}$ acting in the subspace and $\tilde{M}^\pm(l = \text{I-IV}) = \{\pm\Delta_0 + J_0|m|/t_x, \mp\Delta_0 - J_0|m|/t_y, \mp\Delta_0 + J_0|m|/t_x, \pm\Delta_0 - J_0|m|/t_y\}$. It can be found that once J_0 exceeds the critical value $J_c = \Delta_0 t_0/|m|$ (considering the isotropic case $t_x = t_y = t_0$), the signs of the mass terms at the adjacent boundaries in $H^\pm$ are opposite and two mass domain walls are formed at each corner. The zero-energy MCMs formed by H^+ and H^- are decoupled from each
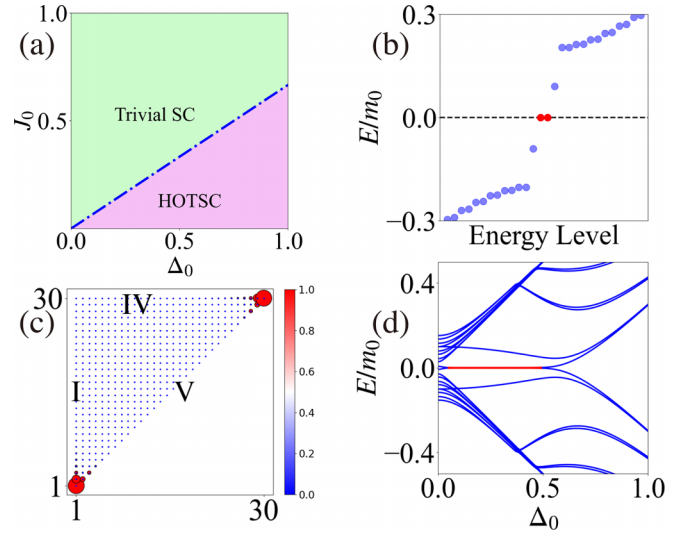

FIG. 3. (a) The phase diagram for the isosceles-right-triangle geometry. (b) The energy spectrum of an isosceles triangle structure with two MCMs (red dots) and the density plot of the two MCMs (c) with V representing the hypotenuse. $\Delta_0 = 0.2$, $J_0 = 0.5$. (d) The real-space energy spectrum evolves with electron-pairing amplitude in the isosceles-right-triangle structure with MCMs marked in red existing in a large range. The common parameters are $m_0 = 1.0$, $t_y = A_y = t_x = A_x = 2.0$, and $\mu = 0.1$.

other, so that two MCMs exist at each corner, as illustrated in Figs. 2(c)–2(e).

Effect of chemical potential. In contrast to the TRS-protected Majorana Kramers pairs [34], only one MZM can stably exist at a given corner without TRS. The chemical potential will give to the edge Hamiltonian (3) a new term $\mu\gamma_z$, which couples the H^+ and H^- sub-blocks. This coupling causes two MCMs from the two sub-blocks at the same corner to mix and disappear. However, two such MCMs are intact if they are located at different corners despite nonzero chemical potential. To demonstrate this effect, we start with an isosceles triangle geometry. We first analyze the situation where $t_x = t_y \equiv t_0$, and we will analyze the situation where $t_x \neq t_y$ later. The altermagnetism causes the Dirac mass $J(\alpha) = J_0 m \cos(2\alpha)/t_0$ at an edge, where α is the angle between the edge and the edge I. For an edge with $\alpha = \pi/4$, i.e., edge V in Fig. 3(c), $J(\alpha) = 0$. Similarly, we can also get the Dirac mass at edge V, $\tilde{M}_V^\pm = \pm\Delta_0$ [64]. By carefully analyzing the signs of the mass terms on the three sides of the sample, we find that when $\Delta_0 < J_0|m|/t_0$, there is a pair of robust MCMs at two vertices of the triangle sample. In the two sub-blocks, the signs of the mass terms read $\text{Sign}[\tilde{M}^+(\text{I, V, IV})] = \{+, +, -\}$ and $\text{Sign}[\tilde{M}^-(\text{I, V, IV})] = \{+, -, -\}$. Note that two adjacent edges with opposite signs will form a domain wall, so there will be a MCM at the intersection. It is useful to define the corner position, corner i-j, which is defined as the intersection of adjacent edge i and edge j. It can be seen that for the H^+ sub-block, there are two MCMs at corner IV-V and corner IV-I, while for the H^- sub-block, there are two MCMs at corner I-V and corner I-IV. The nonzero chemical potential will annihilate a pair of MCMs on the same corner (corner IV-I), with only a pair of stable MCMs at two corners (corner V-I,
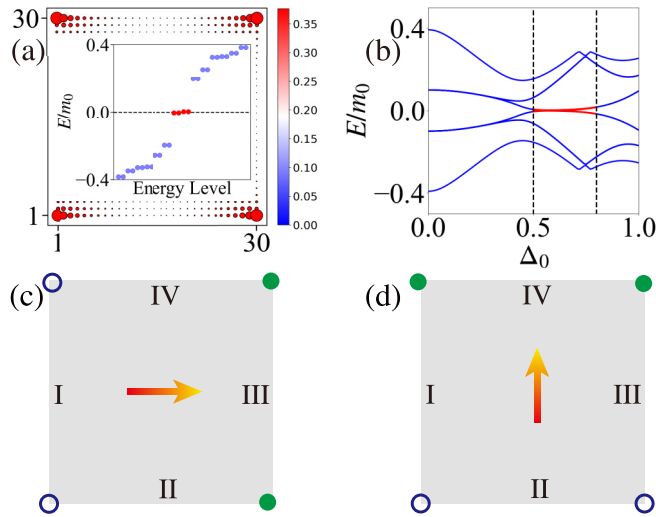
FIG. 4. Results with nonzero chemical potential μ. (a) The real-space wave-function distribution with one MZM localized at each corner. Inset plots the several eigenvalues near zero energy. (b) The real-space energy spectrum evolves with electron-pairing amplitude in a square structure with MCMs marked in red existing in a range. (c), (d) Tunable MCM patterns. The blue hollow (green solid) circles represent the MCMs from the H^+ (H^-) block. The arrows indicate the uniaxial stress direction. The common parameters are $m_0 = 1.0$, $t_y = A_y = 1.0$, $t_x = A_x = 2.0$, $J_0 = \Delta_0 = 0.5$, and $\mu = 0.1$.

corner V-IV). When $\Delta_0 > J_0|m|/t_0$, there is no MCM. These theoretical analyses are also verified by our direct numerical calculations, as shown in Figs. 3(b)–3(d). We also give the phase diagram in Fig. 3(a).

Tunable patterns of MCMs. We discover that uniaxial strain can interestingly manipulate the patterns of the MCMs. We first apply uniaxial stress to a square structure, say along the x direction such that $t_x > t_y$. We find that as the pairing strength increases, the gap of the edge states along the k_y direction of the system is closed and then reopened, but it is always open along the k_x direction, indicating a higher-order topological phase transition [64]. The numerical results in Figs. 4(a) and 4(b) confirm the higher-order topological phase with four highly localized MZMs at each corner. Such results can be understood through edge theory [64]. When $J_0|m|/t_x < \Delta_0 < J_0|m|/t_y$, we obtain, for the two sub-blocks, the signs of the mass terms $\text{Sign}[\tilde{M}^+(l = \text{I} - \text{IV})] = \{+, -, -, -\}$ and $\text{Sign}[\tilde{M}^-(l = \text{I} - \text{IV})] = \{-, -, +, -\}$, respectively. For the H^+ sub-block, there are two MCMs at corner I-IV and corner I-II, while for H^- sub-block, there are two MCMs at corner III-II and corner III-IV. Since the four MCMs are located at four different corners, the nonzero chemical potential does not work, and they can exist stably, as shown in Fig. 4(c). Such an analysis can clearly explain the above numerical results.

We can also apply uniaxial stress along another direction, such as the y direction, such that $t_x < t_y$. We find a higher-order topological phase transition occurs again with one highly localized MZM at each corner [64]. When $J_0|m|/t_y < \Delta_0 < J_0|m|/t_x$, similarly, for the two sub-blocks, the signs of the mass terms read $\text{Sign}[\tilde{M}^\pm(l = \text{I} - \text{IV})] = \{+, \mp, +, \pm\}$.

There are two MCMs at corner II-I (IV-III) and corner II-III (IV-I) for the H^+ (H^-) sub-block. Since the four MCMs are located at four different corners, they can also exist stably despite the nonzero chemical potential, as shown in Fig. 4(d).

It is worth noting that comparing Figs. 4(c) and 4(d), one can find that by changing the uniaxial stress direction, we can interchange two MCMs at corner IV-I and corner II-III. Furthermore, we can also freely move a pair of MCMs spatially to locate at any two vertices of the isosceles structure by applying uniaxial stress [64]. The intriguing properties with tunable patterns of MCMs hold promise for the implementation of Majorana braiding [5] and are particularly useful in the design and fabrication of Majorana systems with desired properties [70].

Discussion. Although altermagnets have been proposed as the third magnetic phase besides ferromagnets and antiferromagnets for a short time, there are already abundant altermagnets available, such as RuO_2 [53,54], KRu_4O_8 [54], and Mn_5Si_3 [55], etc. Recently, spin splitting in altermagnets has been observed by spin- and angle-resolved photoemission spectroscopy measurement [71]. On the other hand, superconducting/topological insulator heterojunctions have been experimentally realized, and induced electron pairing by proximity effect has been observed in topological insulators [72–76]. Consequently, it is evident that the required material ingredients for implementing the proposal are all experimentally accessible. In the experiment, a scanning tunneling microscope can be used to detect MZMs [77], where the differential conductivity peaks at zero energy due to the resonant Andreev reflection are quantized at $2e^2/h$ [78,79]. In addition, the fractional Josephson effect [12] is also strong evidence for the existence of a zero-energy Majorana mode, and anomalous response to radio frequency irradiation produced by a 4π-Josephson current could be observed experimentally [80,81]. The existence of MZMs can be proved by combining the above experimental means.

Our proposal has certain remarkable advantages. First, it does not necessitate the use of unconventional superconductors with small electron coherence lengths and an external magnetic field which make experimental realization and confirmation of the existence of MZMs more difficult. Second, by adjusting the direction of the Néel order parameter of altermagnets, which is readily experimentally, one can create MCMs. In experiments, current, voltage [82,83], and spin-orbit torques [84] can manipulate and detect the direction of the Néel vector in antiferromagnetic materials. Last but not least, altermagnets with zero net magnetization have a non-negligible advantage over conventional magnetic materials when combined with superconductivity [85]. All of these make the experimental realization of the proposal very possible and open a new path for the realization of MCMs.

In addition, the patterns of MCMs implemented by our scheme are flexible and adjustable. For example, for an isosceles triangular structure, a pair of MCMs can be freely moved to any two vertices of the triangle by adjusting uniaxial strain, and for a square structure, two MCMs can be interchanged by adjusting uniaxial strain. These operations are important for braiding MCMs. In particular, we noticed that the triangular

structure hosts a pair of MCMs, so it is equivalent to 1D topological superconductivity nanowires [13,14] and thus can be used to construct T junctions [70] or Y junctions [86–88] for braiding MCMs to exhibit the non-Abelian statistics and potential for topological quantum computation.

[1] J. Alicea, Rep. Prog. Phys. **75**, 076501 (2012).

[2] T. D. Stanescu and S. Tewari, J. Phys.: Condens. Matter **25**, 233201 (2013).

[3] C. Beenakker, Annu. Rev. Condens. Matter Phys. **4**, 113 (2013).

[4] S. R. Elliott and M. Franz, Rev. Mod. Phys. **87**, 137 (2015).

[5] S. D. Sarma, M. Freedman, and C. Nayak, npj Quantum Inf. **1**, 15001 (2015).

[6] M. Sato and S. Fujimoto, J. Phys. Soc. Jpn. **85**, 072001 (2016).

[7] X.-L. Qi and S.-C. Zhang, Rev. Mod. Phys. **83**, 1057 (2011).

[8] M. Sato and Y. Ando, Rep. Prog. Phys. **80**, 076501 (2017).

[9] R. M. Lutchyn, E. P. A. M. Bakkers, L. P. Kouwenhoven, P. Krogstrup, C. M. Marcus, and Y. Oreg, Nat. Rev. Mater. **3**, 52 (2018).

[10] S. M. Frolov, M. J. Manfra, and J. D. Sau, Nat. Phys. **16**, 718 (2020).

[11] S. Das Sarma, Nat. Phys. **19**, 165 (2023).

[12] A. Y. Kitaev, Phys. Usp. **44**, 131 (2001).

[13] Y. Oreg, G. Refael, and F. von Oppen, Phys. Rev. Lett. **105**, 177002 (2010).

[14] R. M. Lutchyn, J. D. Sau, and S. Das Sarma, Phys. Rev. Lett. **105**, 077001 (2010).

[15] N. Read and D. Green, Phys. Rev. B **61**, 10267 (2000).

[16] L. Fu and C. L. Kane, Phys. Rev. Lett. **100**, 096407 (2008).

[17] J. D. Sau, R. M. Lutchyn, S. Tewari, and S. Das Sarma, Phys. Rev. Lett. **104**, 040502 (2010).

[18] J. Alicea, Phys. Rev. B **81**, 125318 (2010).

[19] F. Zhang, C. L. Kane, and E. J. Mele, Phys. Rev. B **86**, 081303(R) (2012).

[20] M. Sitte, A. Rosch, E. Altman, and L. Fritz, Phys. Rev. Lett. **108**, 126807 (2012).

[21] W. A. Benalcazar, B. A. Bernevig, and T. L. Hughes, Science **357**, 61 (2017).

[22] W. A. Benalcazar, B. A. Bernevig, and T. L. Hughes, Phys. Rev. B **96**, 245115 (2017).

[23] Z. Song, Z. Fang, and C. Fang, Phys. Rev. Lett. **119**, 246402 (2017).

[24] J. Langbehn, Y. Peng, L. Trifunovic, F. von Oppen, and P. W. Brouwer, Phys. Rev. Lett. **119**, 246401 (2017).

[25] M. Ezawa, Phys. Rev. Lett. **120**, 026801 (2018).

[26] F. Schindler, Z. Wang, M. G. Vergniory, A. M. Cook, A. Murani, S. Sengupta, A. Y. Kasumov, R. Deblock, S. Jeon, I. Drozdov, H. Bouchiat, S. Guéron, A. Yazdani, B. A. Bernevig, and T. Neupert, Nat. Phys. **14**, 918 (2018).

[27] F. Schindler, A. M. Cook, M. G. Vergniory, Z. Wang, S. S. P. Parkin, B. A. Bernevig, and T. Neupert, Sci. Adv. **4**, eaat0346 (2018).

[28] E. Khalaf, W. A. Benalcazar, T. L. Hughes, and R. Queiroz, Phys. Rev. Res. **3**, 013239 (2021).

[29] M. Geier, L. Trifunovic, M. Hoskam, and P. W. Brouwer, Phys. Rev. B **97**, 205135 (2018).

[30] C.-H. Hsu, P. Stano, J. Klinovaja, and D. Loss, Phys. Rev. Lett. **121**, 196801 (2018).

[31] E. Khalaf, Phys. Rev. B **97**, 205136 (2018).

[32] T. Liu, J. J. He, and F. Nori, Phys. Rev. B **98**, 245413 (2018).

[33] H. Shapourian, Y. Wang, and S. Ryu, Phys. Rev. B **97**, 094508 (2018).

[34] Q. Wang, C.-C. Liu, Y.-M. Lu, and F. Zhang, Phys. Rev. Lett. **121**, 186801 (2018).

[35] Z. Yan, F. Song, and Z. Wang, Phys. Rev. Lett. **121**, 096803 (2018).

[36] X. Zhu, Phys. Rev. B **97**, 205134 (2018).

[37] X. Zhu, Phys. Rev. Lett. **122**, 236401 (2019).

[38] Z. Yan, Phys. Rev. Lett. **123**, 177001 (2019).

[39] R.-X. Zhang, W. S. Cole, and S. Das Sarma, Phys. Rev. Lett. **122**, 187001 (2019).

[40] X.-H. Pan, K.-J. Yang, L. Chen, G. Xu, C.-X. Liu, and X. Liu, Phys. Rev. Lett. **123**, 156801 (2019).

[41] Y. Peng and G. Refael, Phys. Rev. Lett. **123**, 016806 (2019).

[42] R.-X. Zhang, W. S. Cole, X. Wu, and S. Das Sarma, Phys. Rev. Lett. **123**, 167001 (2019).

[43] M. J. Gray, J. Freudenstein, S. Y. F. Zhao, R. O'Connor, S. Jenkins, N. Kumar, M. Hoek, A. Kopec, S. Huh, T. Taniguchi, K. Watanabe, R. Zhong, C. Kim, G. D. Gu, and K. S. Burch, Nano Lett. **19**, 4890 (2019).

[44] M. Kheirkhah, Z. Yan, Y. Nagai, and F. Marsiglio, Phys. Rev. Lett. **125**, 017001 (2020).

[45] D. D. Vu, R.-X. Zhang, and S. Das Sarma, Phys. Rev. Res. **2**, 043223 (2020).

[46] F. Schindler, B. Bradlyn, M. H. Fischer, and T. Neupert, Phys. Rev. Lett. **124**, 247001 (2020).

[47] Y.-J. Wu, J. Hou, Y.-M. Li, X.-W. Luo, X. Shi, and C. Zhang, Phys. Rev. Lett. **124**, 227001 (2020).

[48] S. Ikegaya, W. B. Rui, D. Manske, and A. P. Schnyder, Phys. Rev. Res. **3**, 023007 (2021).

[49] S. Qin, C. Fang, F.-C. Zhang, and J. Hu, Phys. Rev. X **12**, 011030 (2022).

[50] X. Wu, X. Liu, R. Thomale, and C.-X. Liu, Natl. Sci. Rev. **9**, nwab087 (2022).

[51] L. Šmejkal, J. Sinova, and T. Jungwirth, Phys. Rev. X **12**, 040501 (2022).

[52] L. Šmejkal, A. H. MacDonald, J. Sinova, S. Nakatsuji, and T. Jungwirth, Nat. Rev. Mater. **7**, 482 (2022).

[53] K.-H. Ahn, A. Hariki, K.-W. Lee, and J. Kuneš, Phys. Rev. B **99**, 184432 (2019).

[54] L. Šmejkal, J. Sinova, and T. Jungwirth, Phys. Rev. X **12**, 031042 (2022).

[55] H. Reichlová, R. L. Seeger, R. González-Hernández, I. Kounta, R. Schlitz, D. Kriegner, P. Ritzinger, M. Lammel, M. Leiviskä, V. Petříček, P. Doležal, E. Schmoranzerová, A. Bad'ura, A. Thomas, V. Baltz, L. Michez, J. Sinova, S. T. B. Goennenwein, T. Jungwirth, and L. Šmejkal, arXiv:2012.15651.

[56] H.-Y. Ma, M. Hu, N. Li, J. Liu, W. Yao, J.-F. Jia, and J. Liu, Nat. Commun. **12**, 2846 (2021).

[57] I. I. Mazin, K. Koepernik, M. D. Johannes, R. González-Hernández, and L. Šmejkal, Proc. Natl. Acad. Sci. USA **118**, e2108924118 (2021).

[58] Z. Feng, X. Zhou, L. Šmejkal, L. Wu, Z. Zhu, H. Guo, R. González-Hernández, X. Wang, H. Yan, P. Qin, X. Zhang, H. Wu, H. Chen, Z. Xia, C. Jiang, M. Coey, J. Sinova, T. Jungwirth, and Z. Liu, Nat. Electron. **5**, 735 (2022).

[59] R. D. Gonzalez Betancourt, J. Zubáč, R. Gonzalez-Hernandez, K. Geishendorf, Z. Šobáň, G. Springholz, K. Olejník, L. Šmejkal, J. Sinova, T. Jungwirth, S. T. B. Goennenwein, A. Thomas, H. Reichlová, J. Železný, and D. Kriegner, Phys. Rev. Lett. **130**, 036702 (2023).

[60] I. I. Mazin, Phys. Rev. B **107**, L100418 (2023).

[61] C. Sun, A. Brataas, and J. Linder, Phys. Rev. B **108**, 054511 (2023).

[62] S.-B. Zhang, L.-H. Hu, and T. Neupert, arXiv:2302.13185.

[63] X. Zhou, W. Feng, R.-W. Zhang, L. Smejkal, J. Sinova, Y. Mokrousov, and Y. Yao, arXiv:2305.01410.

[64] See Supplemental Material at http://link.aps.org/supplemental/10.1103/PhysRevB.108.205410 for more details about (I) the derivation of the edge Hamiltonian for square and isosceles right triangular structures when the Néel vector is oriented in any direction, with special attention paid to the situation with the Néel vector in the z direction. The effective boundary Hamiltonian for the cases of altermagnets with g-wave and i-wave spin splitting is derived. (II) The variation of the number of MCMs under anisotropy and finite chemical potential in the square structure is studied. (III) Manipulation of MCMs in square and isosceles right triangular structures under the influence of uniaxial stress, which includes Refs. [34,39,52,54,89].

[65] L. Šmejkal, J. Železný, J. Sinova, and T. Jungwirth, Phys. Rev. Lett. **118**, 106402 (2017).

[66] C. L. Kane and E. J. Mele, Phys. Rev. Lett. **95**, 146802 (2005).

[67] B. A. Bernevig, T. L. Hughes, and S.-C. Zhang, Science **314**, 1757 (2006).

[68] L. Fu and C. L. Kane, Phys. Rev. B **76**, 045302 (2007).

[69] The in-plane Néel vector does not generate a Dirac mass on the edge.

[70] J. Alicea, Y. Oreg, G. Refael, F. von Oppen, and M. P. A. Fisher, Nat. Phys. **7**, 412 (2011).

[71] Y.-P. Zhu, X. Chen, X.-R. Liu, P. Liu, H. Zha, C. Hong, J. Li, Z. Jiang, X.-M. Ma, Y.-J. Hao, W. Liu, M. Zeng, J. Ding, S. Mo, Z. Liu, M. Ye, D. Shen, R.-H. He, S. Qiao, Q. Liu *et al.*, arXiv:2303.04549.

[72] E. Wang, H. Ding, A. V. Fedorov, W. Yao, Z. Li, Y.-F. Lv, K. Zhao, L.-G. Zhang, Z. Xu, J. Schneeloch, R. Zhong, S.-H. Ji, L. Wang, K. He, X. Ma, G. Gu, H. Yao, Q.-K. Xue, X. Chen, and S. Zhou, Nat. Phys. **9**, 621 (2013).

[73] J.-P. Xu, C. Liu, M.-X. Wang, J. Ge, Z.-L. Liu, X. Yang, Y. Chen, Y. Liu, Z.-A. Xu, C.-L. Gao, D. Qian, F.-C. Zhang, and J.-F. Jia, Phys. Rev. Lett. **112**, 217001 (2014).

[74] H. Zhao, B. Rachmilowitz, Z. Ren, R. Han, J. Schneeloch, R. Zhong, G. Gu, Z. Wang, and I. Zeljkovic, Phys. Rev. B **97**, 224504 (2018).

[75] N. Shimamura, K. Sugawara, S. Sucharitakul, S. Souma, K. Iwaya, K. Nakayama, C. X. Trang, K. Yamauchi, T. Oguchi, K. Kudo, T. Noji, Y. Koike, T. Takahashi, T. Hanaguri, and T. Sato, ACS Nano **12**, 10977 (2018).

[76] F. Lüpke, D. Waters, S. C. de la Barrera, M. Widom, D. G. Mandrus, J. Yan, R. M. Feenstra, and B. M. Hunt, Nat. Phys. **16**, 526 (2020).

[77] B. Jäck, Y. Xie, J. Li, S. Jeon, B. A. Bernevig, and A. Yazdani, Science **364**, 1255 (2019).

[78] K. T. Law, P. A. Lee, and T. K. Ng, Phys. Rev. Lett. **103**, 237001 (2009).

[79] M. Wimmer, A. R. Akhmerov, J. P. Dahlhaus, and C. W. J. Beenakker, New J. Phys. **13**, 053016 (2011).

[80] L. P. Rokhinson, X. Liu, and J. K. Furdyna, Nat. Phys. **8**, 795 (2012).

[81] J. Wiedenmann, E. Bocquillon, R. S. Deacon, S. Hartinger, O. Herrmann, T. M. Klapwijk, L. Maier, C. Ames, C. Brüne, C. Gould, A. Oiwa, K. Ishibashi, S. Tarucha, H. Buhmann, and L. W. Molenkamp, Nat. Commun. **7**, 10303 (2016).

[82] J. Godinho, H. Reichlová, D. Kriegner, V. Novák, K. Olejník, Z. Kašpar, Z. Šobáň, P. Wadley, R. P. Campion, R. M. Otxoa, P. E. Roy, J. Železný, T. Jungwirth, and J. Wunderlich, Nat. Commun. **9**, 4686 (2018).

[83] A. Mahmood, W. Echtenkamp, M. Street, J.-L. Wang, S. Cao, T. Komesu, P. A. Dowben, P. Buragohain, H. Lu, A. Gruverman, A. Parthasarathy, S. Rakheja, and C. Binek, Nat. Commun. **12**, 1674 (2021).

[84] P. Zhang, C.-T. Chou, H. Yun, B. C. McGoldrick, J. T. Hou, K. A. Mkhoyan, and L. Liu, Phys. Rev. Lett. **129**, 017203 (2022).

[85] M. G. Blamire and J. W. A. Robinson, J. Phys.: Condens. Matter **26**, 453201 (2014).

[86] D. J. Clarke, J. D. Sau, and S. Tewari, Phys. Rev. B **84**, 035120 (2011).

[87] T. Hyart, B. van Heck, I. C. Fulga, M. Burrello, A. R. Akhmerov, and C. W. J. Beenakker, Phys. Rev. B **88**, 035121 (2013).

[88] L.-H. Wu, Q.-F. Liang, and X. Hu, Sci. Technol. Adv. Mater. **15**, 064402 (2014).

[89] R. Jackiw and C. Rebbi, Phys. Rev. D **13**, 3398 (1976).